Search for non-Gaussianity in pixel, harmonic, and wavelet space: Compared and combined

Paolo Cabella,[1,*] Frode Hansen,[1,†] Domenico Marinucci,[2,‡] Daniele Pagano,[1]
and Nicola Vittorio[1]

[1]*Dipartimento di Fisica, Università di Roma "Tor Vergata," Via della Ricerca Scientifica 1, I-00133 Roma, Italy*
[2]*Dipartimento di Matematica, Università di Roma "Tor Vergata," Via della Ricerca Scientifica 1, I-00133 Roma, Italy*

(Received 8 July 2003; revised manuscript received 2 December 2003; published 25 March 2004)

We present a comparison between three approaches to test the non-Gaussianity of cosmic microwave background data. The Minkowski functionals, the empirical process method, and the skewness of wavelet coefficients are applied to maps generated from nonstandard inflationary models and to Gaussian maps with point sources included. We discuss the different power of the pixel, harmonic, and wavelet space methods on these simulated almost full-sky data (with Planck-like noise). We also suggest a new procedure consisting of a combination of statistics in pixel, harmonic, and wavelet space.

DOI: 10.1103/PhysRevD.69.063007 PACS number(s): 95.75.Pq, 02.50.Ng, 02.50.Tt, 98.80.Es

I. INTRODUCTION

The fluctuations of the cosmic microwave background (CMB) are expected to be close to Gaussian distributed. In view of the increasing quantity of CMB experiments, it is now possible to check this assumption on data with a growing resolution and sky coverage. Most models for the early Universe predict some small deviations from Gaussianity: nonstandard models of inflation [1–7], cosmic strings (see Ref. [8] for a review), and point sources. Detecting these small deviations would be of great importance for the understanding of the physics of the early Universe. Systematic effects such as a nonsymmetric beam and noise could also give rise to non-Gaussian features. For this reason a non-Gaussianity check could reveal whether the impact of instrumental effects on the data of the experiment is well understood.

The methods to search for non-Gaussianity in the literature mainly concentrate on implementing the test in three different spaces. (1) In pixel space, the Minkowski functionals [9,10] [which were used to set limits on the non-Gaussianity in the Wilkinson Microwave Anisotropy Probe (WMAP) data [11]], temperature correlation functions [12], the peak to peak correlation function [13], skewness and kurtosis of the temperature field [14], and curvature properties [15,16] are used, to mention a few. (2) In harmonic space, the bispectrum and its normalized version [17–20] and the bispectrum in the flat sky approximation [21] can be analyzed. The explicit form of the trispectrum for CMB data was derived in [22,23]. Phase mapping can be used [24]. Applications to Cosmic Background Explorer (COBE), Maxima, and Boomerang data have also drawn enormous attention and raised wide debate [25–28]. The empirical process method is used [29–31]. Finally, (3) tests in wavelet space [32–35]. Traditionally, these tests are performed separately in each space. In this article, we will take methods in pixel (the Minkowski functionals), harmonic (the empirical process), and wavelet space (skewness), and we will make a comparison for two different models of non-Gaussianity. We will also combine the methods in order to improve the total power. It should be noted that all the procedures we consider are nonparametric; that is, they do not assume any *a priori* knowledge about the nature of non-Gaussianity.

We will use these methods on 100 maps generated from a nonstandard inflationary model [6] and on 100 maps where we have included point sources. We assess the performance of the methods in the different spaces for the different types of non-Gaussianity. We also propose a combined test which turns out to be more robust.

In Sec. II, we review the method of Minkowski functionals, in Sec. III we describe our implementation of the method, and in Sec. IV we define our proposed statistic. In Sec. V we review the empirical process method while Sec. VI is devoted to the wavelets. In Sec. VII the methods are compared and applied to nonstandard inflationary models; and in Sec. VIII to maps with point sources. Finally, in Sec. IX we summarize and comment on our results.

II. MINKOWSKI FUNCTIONALS

To analyze a spherical map in terms of Minkowski functionals, we consider the excursion sets, that is, the map subsets which exceed a given threshold value. The threshold is labeled ν, and it is treated as an independent variable, on which these functionals depend. More precisely, considering the normalized random field of temperature fluctuations, $u = \Delta T/\sigma(\Delta T)$; we can define the "hot region" Q as the ensemble of pixels u_i higher than the ν level:

$$Q \equiv Q(\nu) = \{i | u(\theta_i, \varphi_i) > \nu\}. \tag{1}$$

The three functionals of interest then are, up to constant factors [36],

(1) *area:* $M_0(\nu)$ is the total area of all hot regions;

(2) *boundary length:* $M_1(\nu)$ is proportional to the total length of the boundary between cold and hot regions; and

(3) *Euler characteristic or genus:* $M_2(\nu)$, a purely topological quantity, counts the number of isolated hot regions

*Electronic address: Paolo.Cabella@roma2.infn.it
†Electronic address: frodekh@roma2.infn.it
‡Electronic address: marinucc@mat.uniroma2.it

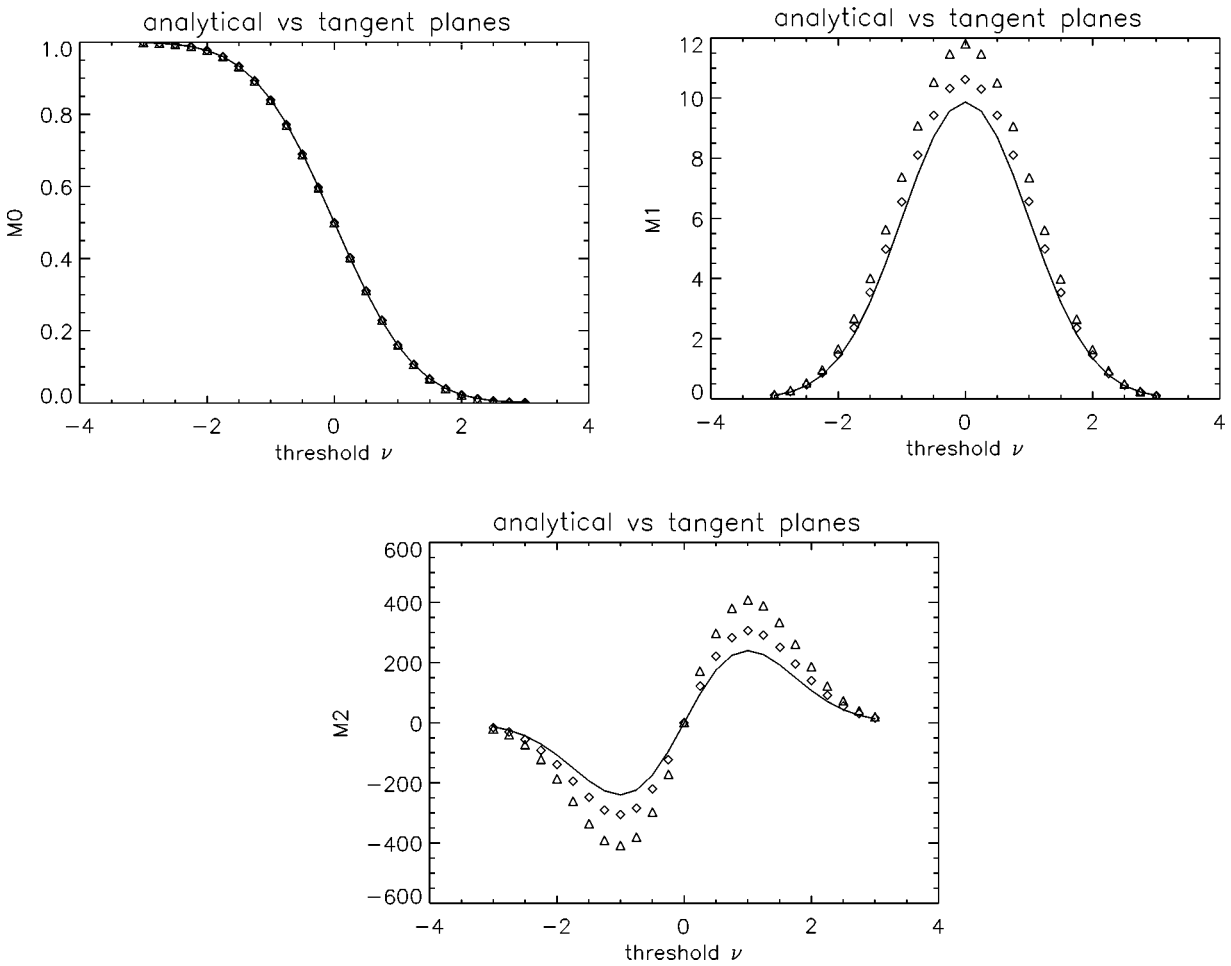

FIG. 1. A comparison between a Gaussian map (solid line) and a non-Gaussian map with $f_{NL}=1000$ (squares) (the f_{NL} factor will be explained in Sec. VII).

minus the number of isolated cold regions, i.e., the number of connected components in Q minus the number of ''holes.''

The rationale behind these statistics can be explained from mathematical results in [45]; in particular, these results can be interpreted by stating that all the morphological information of a convex body is contained in the Minkowski functionals [46]; here, by ''morphological'' we mean the properties that are invariant under translations and rotations and are additive [37–39]. The three statistics, normalized by the area density, can then be expressed as

$$M_0(\nu)=\frac{1}{A}\int_Q dA, \tag{2}$$

$$M_1(\nu)=\frac{1}{4A}\int_{\partial Q} dl, \tag{3}$$

$$M_2(\nu)=\frac{1}{2\pi A}\int_{\partial Q}\kappa\, dl, \tag{4}$$

where ∂Q is the contour of the region Q; dA and dl are the differential elements of Q and ∂Q, respectively; κ is the geodetic curvature of dl.

The expected value for a given threshold depends on a single parameter τ given for a Gaussian field by [39]

$$M_0(\nu)=\frac{1}{2}\left[1-\mathrm{erf}\left(\frac{\nu}{\sqrt{(2)}}\right)\right], \tag{5}$$

$$M_1(\nu)=\frac{\sqrt{\tau}}{8}\exp\left(-\frac{\nu^2}{2}\right), \tag{6}$$

$$M_2(\nu)=\frac{\tau}{\sqrt{8\pi^3}}\nu\exp\left(-\frac{\nu^2}{2}\right), \tag{7}$$

with

$$\tau=\frac{1}{2}\langle u_{;i}u_{;i}\rangle, \tag{8}$$

where the semicolon indicates the covariant derivative on the sphere.

In the case of the CMB (8) reduces to [38]

$$\tau=\sum_{l=1}^{\infty}(2l+1)C_\ell\frac{l(l+1)}{2} \tag{9}$$

where C_ℓ is the angular power spectrum.

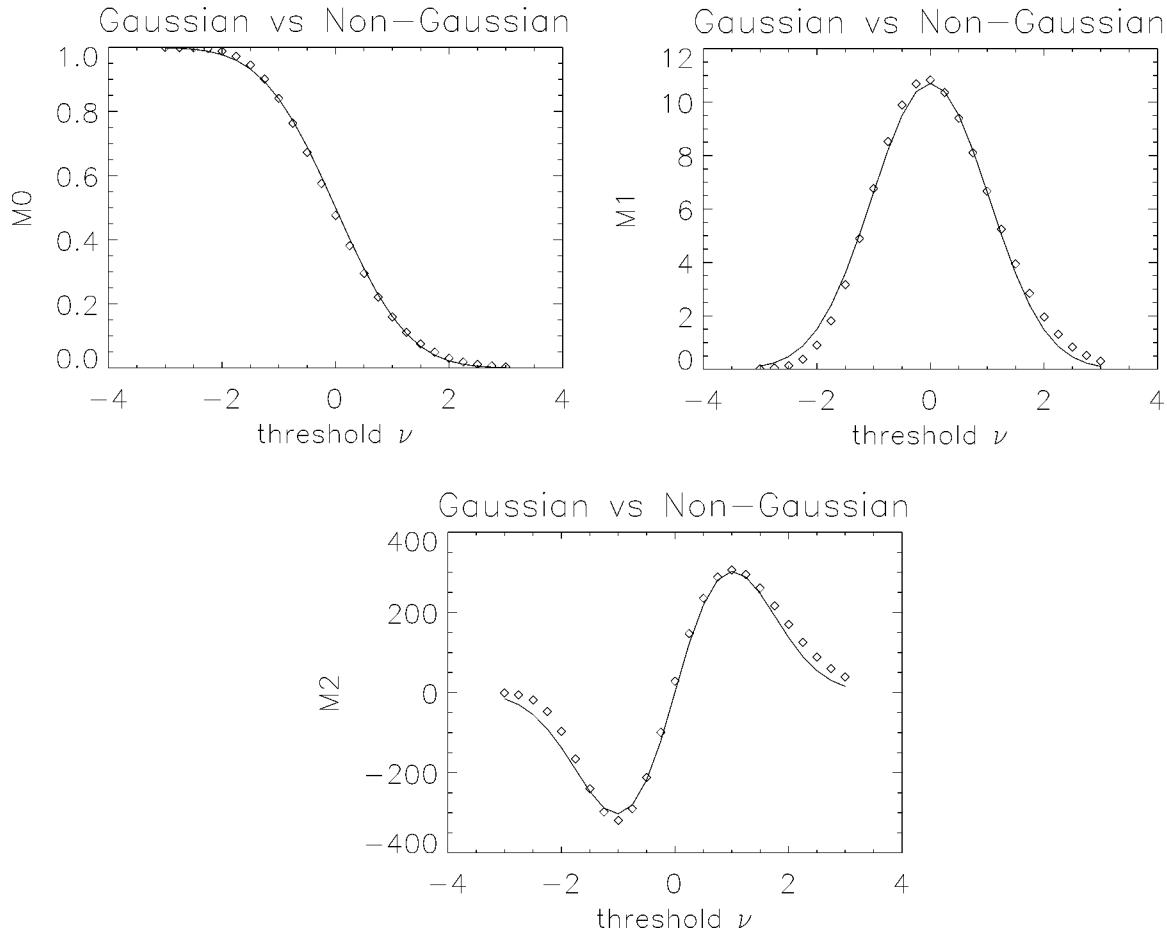

FIG. 2. Comparison between Minkowski functionals computed in the tangent plane approximation and their analytical predictions (solid line) [see Eq. (5)]. Squares refer to tangent planes of size $\simeq(12°\times12°)$, triangles refer to tangent planes of size $\simeq(24°\times24°)$.

An immediate consequence of the above formulas is that, although the expected value of the first Minkowski functional is invariant with respect to the dependence structure of ΔT, for the second and third Minkowski functionals this is not the case and calibration for a given angular power spectrum C_ℓ is needed. Moreover, even for the first Minkowski functional, knowledge of the angular power spectrum is required for a Monte Carlo evaluation of its variance. This can be viewed as a drawback, and because of this some effort has been undertaken to provide at least some crude upper bound for the functionals' variance [46].

III. THE IMPLEMENTATION OF MINKOWSKI FUNCTIONALS

In order to estimate the three functionals we simulate a map of the CMB [40] with a known power spectrum, and then we cut the maximum number of independent tangent planes of dimension $\simeq12°\times12°$; in this way it is easy to calculate the values of the three Minkowski functionals in the flat-sky limit, taking into account the possibility of gaps (galactic cuts, polar calottes). Due to projection effects, finite pixel size, and the dimension of the tangent planes, we find a deviation of the simulated values with respect to the analytical spherical predictions [Eq. (5)]. Note, however, that the shape of the curves is unaffected, which is not the case when non-Gaussianities are present (see Fig. 1). In Fig. 2 we show a comparison between analytical expectation values and the values computed on the tangent planes.

IV. TEST OF NON-GAUSSIANITY IN PIXEL SPACE

In order to test non-Gaussianity we use a test defined by

$$I_i=\int |M^i(\nu)-\overline{M}^i(\nu)|d\nu, \quad i=0,1,2. \tag{10}$$

Our procedure is as follows.

Given an observed map, we estimate the power spectrum.

Using the estimated power spectrum, we generate 200 Gaussian realizations [40].

For each map we calculate the Minkowski functionals, using the tangent planes as described above.

We calibrate the quantiles (i.e., the threshold values at a given significance level) using Monte Carlo simulations; the one and two sigma detection levels are shown in Fig. 3.

We calculate our statistic (10) from the observed map and compare the result with the Monte Carlo calibration; we are thus able to determine at what confidence level the map is or is not Gaussian.

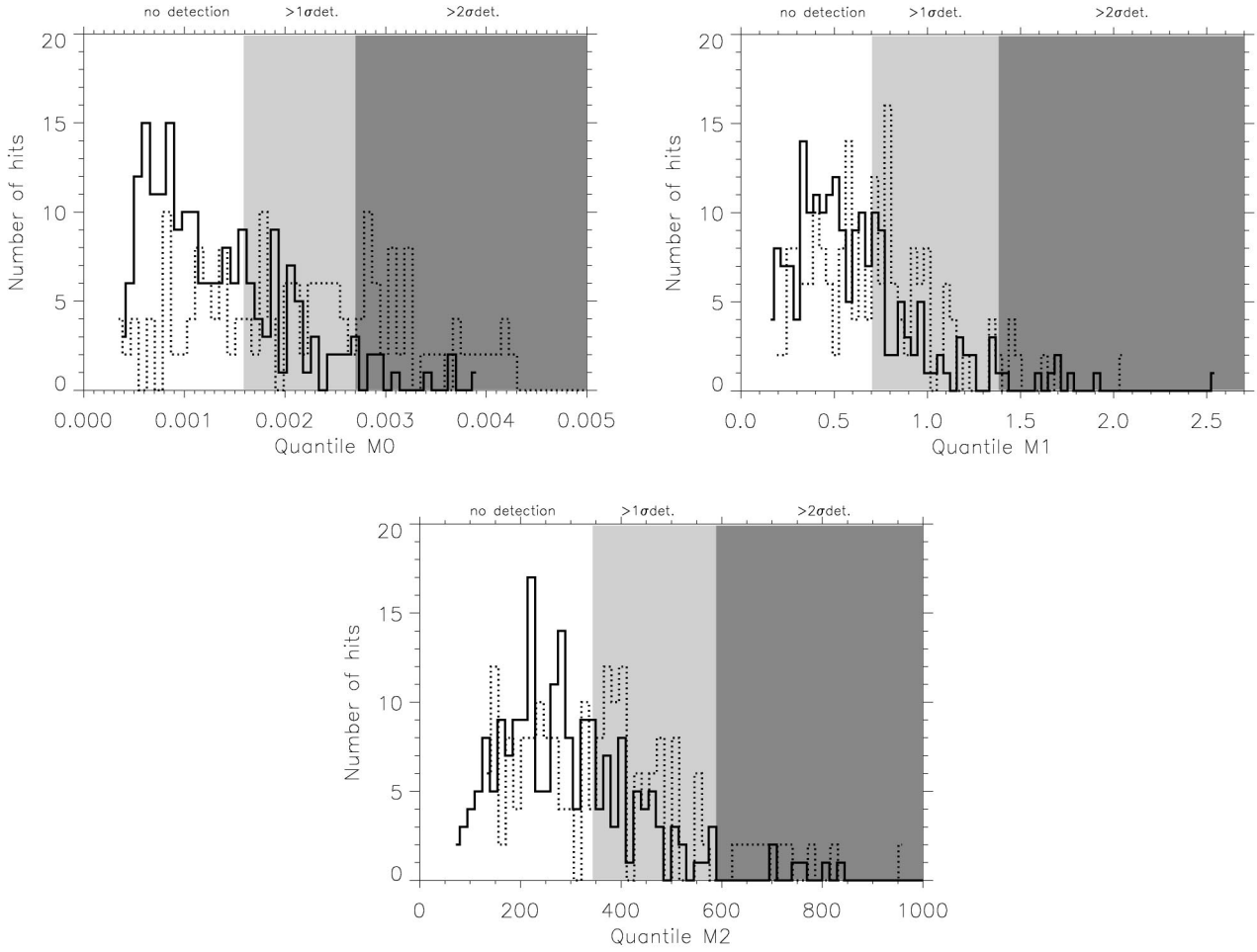

FIG. 3. Histogram with threshold levels for all three Minkowski functionals for Gaussian realizations (solid line) and non-Gaussian realizations with $f_{NL}=100$ (dotted line) (the f_{NL} factor will be explained in Sec. VII). All realizations have Planck-like noise and beam 20′. The shaded areas represent the 1σ and 2σ detection limits.

V. THE EMPIRICAL PROCESS METHOD

The details of the empirical process approach to detecting non-Gaussianity in the CMB were given in [29–31]. In short, the method consists of a family of tests which focus on the total distribution of $a_{\ell m}$ and check for dependencies between k ℓ-rows. The first step is to transform the spherical harmonic coefficients into variables $u_{\ell m}$ which have an approximately uniform distribution between 0 and 1, given that the $a_{\ell m}$ were initially Gaussian distributed. This is done using the Smirnov transformation, defined as

$$u_{\ell 0}=\Phi_1\left(\frac{|a_{\ell 0}|^2}{\hat{C}_\ell}\right), \quad u_{\ell m}=\Phi_2\left(\frac{2|a_{\ell m}|^2}{\hat{C}_\ell}\right),$$

$$m=1,2,\ldots,l, \quad l=1,2,\ldots L,$$

where Φ_n is the cumulative distribution function of a χ^2 with n degrees of freedom, and $\hat{C}_\ell$ are the power spectrum coefficients estimated from the data. The error introduced by using an estimated $\hat{C}_\ell$ instead of the real underlying C_ℓ is dealt with using a bias subtraction, as described in [29].

Then the joint empirical distribution function for row ℓ is formed,

$$\hat{F}_{\ell,\ldots,\ell+\Delta_{\ell,k-1}}(\alpha_1,\ldots,\alpha_k) = \frac{1}{(\ell+1)}\sum_{m=0}^{\ell}\left\{\mathbf{1}(\hat{u}_{\ell m}\leqslant\alpha_1)\times\prod_{i=2}^{k}\mathbf{1}(\hat{u}_{\ell+\Delta_{\ell,i-1},m+\Delta_{mi}}\leqslant\alpha_i)\right\},$$

$$\Delta_{mi}\geqslant 0,$$

where $\Delta_{\ell,i}$ determines the spacing between the rows for which the dependencies are tested and Δ_{mi} denotes the difference in m for row i. The parameters α_i run over the interval $[0,1]$. The empirical process is expressed using the centered and rescaled $\hat{F}_{\ell,\ldots,\ell+\Delta_{\ell,k-1}}$ given as

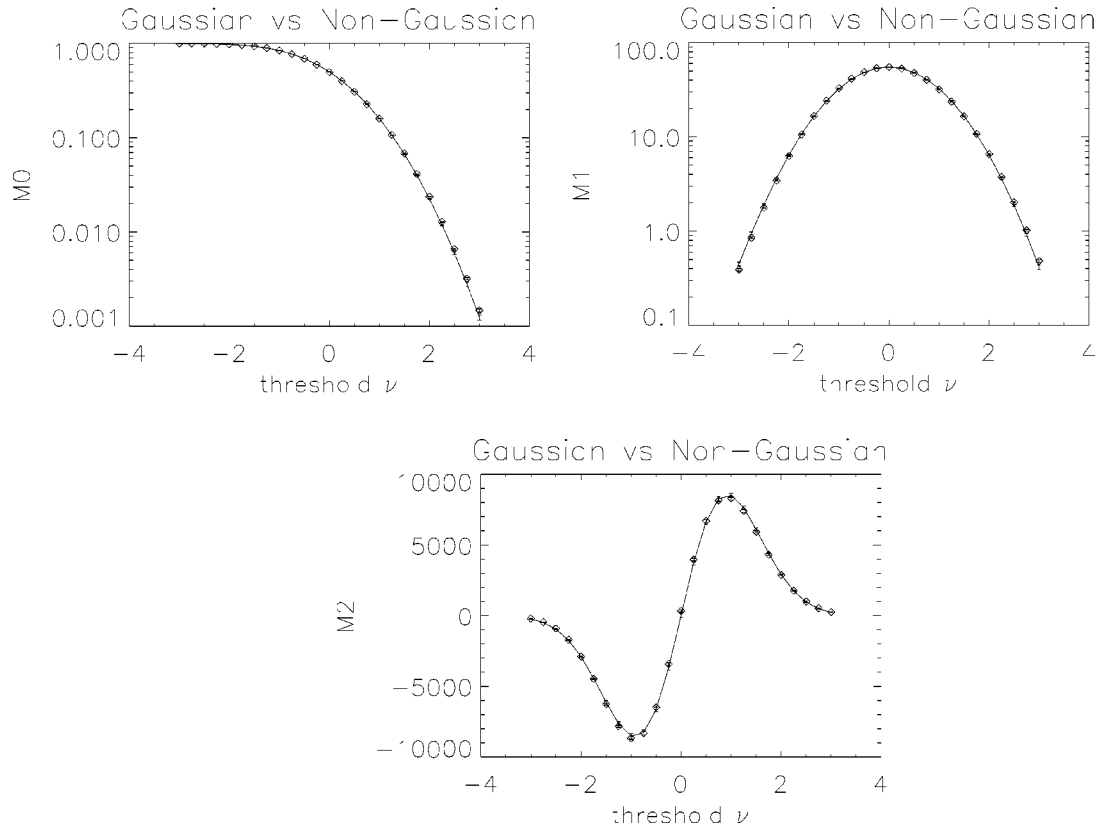

FIG. 4. Minkowski functionals averaged over 200 realizations of Gaussian maps (solid line) and 100 non-Gaussian maps (squares) with $f_{NL}=300$, Planck noise, and beam $20'$. The small 1σ deviations are also shown.

$$\hat{G}_{\ell,\ldots,\ell+\Delta_{\ell,k-1}}(\alpha_1,\ldots,\alpha_k) = \sqrt{(\ell+1)}\left\{\hat{F}_{\ell,\ldots,\ell+\Delta_{\ell,k-1}}(\alpha_1,\ldots,\alpha_k)-\prod_{i=1}^{k}\alpha_i\right\}.$$

The intuition behind this procedure is as follows. If the $a_{\ell m}$'s are Gaussian, $\hat{G}$ converges to a well-defined limiting process, whose distribution can be readily tabulated. On the other hand, for non-Gaussian $a_{\ell m}$'s $\{\hat{F}(\alpha_1,\ldots,\alpha_k) - \Pi_{i=1}^{k}\alpha_i\}$ and thereby $\hat{G}$ will take "high" values over some parts of α space. Thus, the analysis of some appropriate functional of $\hat{G}$ can be used to detect non-Gaussianity. To combine the information over all multipoles into one statistic, we define

$$\hat{K}_L(\alpha_1,\ldots,\alpha_k,r) = \frac{1}{\sqrt{L-\Delta_{\ell,k-1}}} \times \sum_{\ell=1}^{[(L-\Delta_{k-1})r]} \hat{G}_{\ell,\ldots,\ell+\Delta_{\ell,k-1}}(\alpha_1,\ldots,\alpha_k), \tag{11}$$

where L is the highest multipole where the data are signal dominated.

The method can then be summarized as follows. The distribution of $\sup|\hat{K}_L|$ is found using Monte Carlo simulations of Gaussian distributed $a_{\ell m}$. Then, for a given observed set of $a_{\ell m}$, the value $k_{\max}=\sup|\hat{K}_L|$ is found and compared to the distribution obtained from the Monte Carlo simulation. The consistency of the data with a Gaussian distribution can then be estimated to any suitable σ level. In [30] this simple approach was extended in three different ways. First of all, the fact that the above explained estimator is not rotationally invariant was exploited, using the $k_{\max}$ value averaged over many rotations. Each rotation can be viewed as a resampling of the $a_{\ell m}$. Secondly, we introduced three variations of the test, taking into account not only the modulus of the $a_{\ell m}$ but also the phases. Finally, experimental effects like noise and galactic cuts were accounted for using Monte Carlo calibration of the $k_{\max}$ distribution with these effects included. It should be noted that the rotated maps are clearly dependent, and the resulting statistic may thus depend on the shape of the angular power spectrum.

VI. TEST OF NON-GAUSSIANITY IN WAVELET SPACE

A third space where one could look for non-Gaussianity is the wavelet space. The use of wavelets for non-Gaussianity tests of the CMB has been investigated by several authors [32–35] and it turns out to be a very powerful tool. We will here just briefly describe the wavelet method, and refer to the above references for more details.

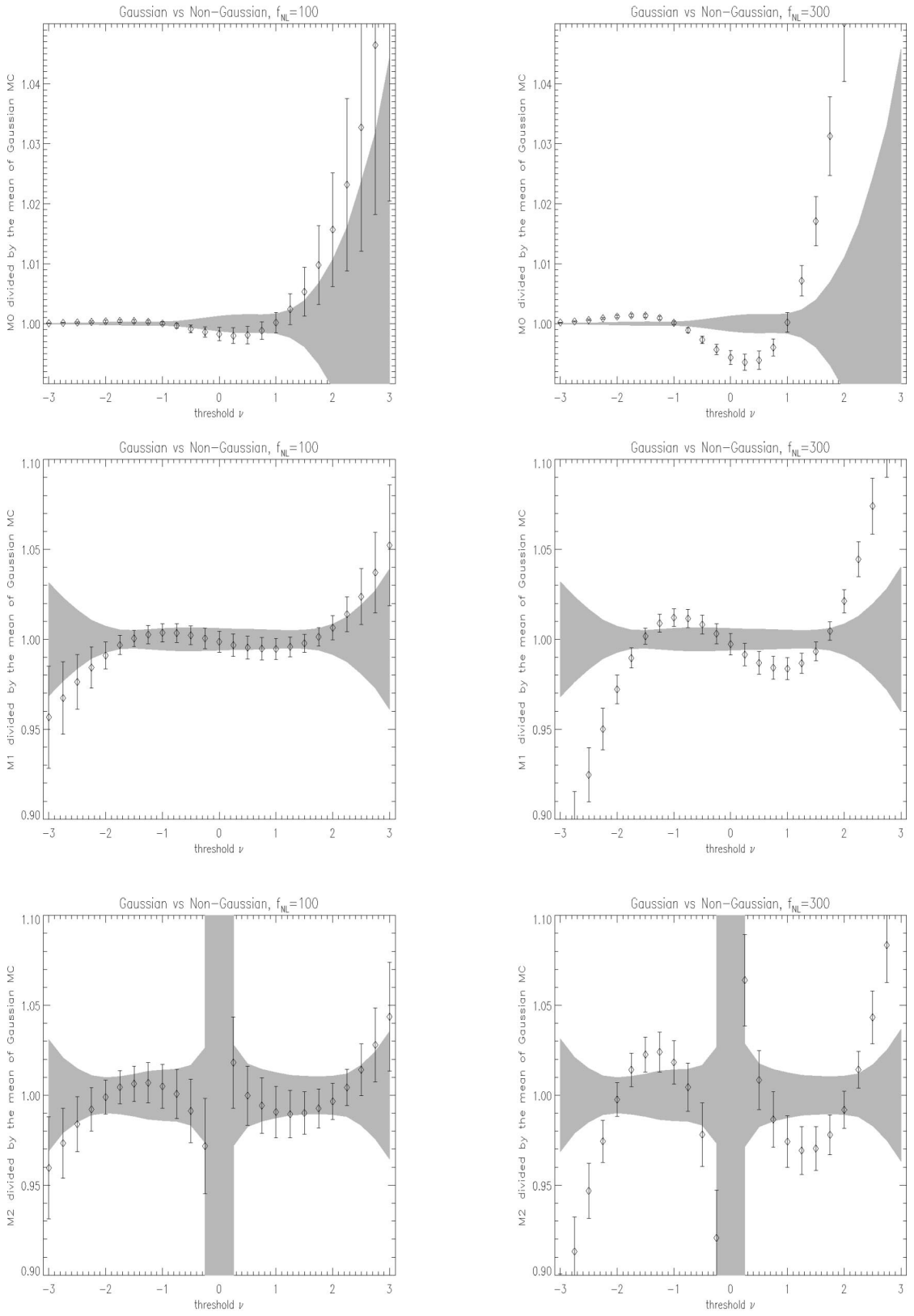

FIG. 5. Minkowski functionals (divided by the mean) averaged over 200 realizations of Gaussian maps (solid line) and 100 non-Gaussian maps (squares) with $f_{NL}=300/100$, Planck noise, and beam $20'$. The shaded bands show the 1σ deviations of the Gaussian realizations, and the error bars show the 1σ deviations for the non-Gaussian maps.

TABLE I. The quantile levels which determine the 1σ and 2σ detections and the rejection rates for nonstandard inflationary models with $f_{NL}=300$.

Quantile detection limits								
I_0	1σ	3.6×10^{-3}	I_1	1σ	0.286	I_2	1σ	33.2
	2σ	6.3×10^{-3}		2σ	0.524		2σ	49.7
Rejection rates (%)								
I_0	1σ	100	I_1	1σ	100	I_2	1σ	100
	2σ	100		2σ	71		2σ	84

An isotropic wavelet can be defined as

$$\Psi(\vec{x};\vec{b},R)=\frac{1}{R}\psi\left(\frac{|\vec{x}-\vec{b}|}{R}\right) \tag{12}$$

with the properties

$$\int d\vec{x}\,\psi(x)=0, \tag{13}$$

$$\int d\omega\,\frac{\psi^2(\omega)}{\omega}<\infty, \tag{14}$$

where $x=|\vec{x}|$, and R represents a scale and b a translation. The Fourier transform of the wavelet is represented by $\psi(\omega)$. We will focus on the Mexican hat wavelets given by

$$\Psi(\vec{x};\vec{b},R)=\frac{1}{(2\pi)^{1/2}R}\left[2-\left(\frac{|\vec{x}-\vec{b}|}{R}\right)^2\right]e^{-|\vec{x}-\vec{b}|^2/2R^2}. \tag{15}$$

From the wavelet transform of a function $f(\vec{x})$ one can obtain the wavelet coefficients

$$w(\vec{b},R)=\int d\vec{x}\,\psi(\vec{x};\vec{b},R)f(\vec{x}) \tag{16}$$

and, if $f(\vec{x})$ is Gaussian, $w(\vec{b},R)$ will be Gaussian as well. We will here use the CMB temperature fluctuation field as the $f(\vec{x})$ function. We will implement the non-Gaussianity test in wavelet space as we did for the Minkowski functionals.

We generate a set of Gaussian CMB maps for calibration and a set of non-Gaussian maps for testing.

We cut tangent planes ($12°\times12°$).

We calculate for each plane the coefficients $w(\vec{b},R)$.

We evaluate the skewness of the wavelet coefficients for each sky.

Finally, using the skewness of the wavelets from the Gaussian maps, we define the 1σ and 2σ detection levels as described above for the other methods.

VII. COMPARISON AND COMBINED TEST

This section aims at comparing the different methods described above. Applying the methods on the same maps, we will first compare the number of detections. We will in this paper use the nonstandard inflationary model described in [6,7], which has the nonlinear coupling parameter f_{NL} as a measure of the strength of non-Gaussianity. We generated 100 ''observed'' skies with Planck-like noise [low frequency instrument (LFI) 100 GHz], beam $20'$, pixel size $\simeq 6'$ (Nside 512 in HEALPIX language), using a pure Sachs-Wolfe spectrum with f_{NL} values of 300 and 100. In Figs. 1, 4, and 5 one can see the behavior of the Minkowski functionals in the presence of a nonzero f_{NL}. In Tables I and II we show the rejection rates. As the first Minkowski functional gave the best results in this test, we will focus only on M_0 for this kind of non-Gaussianity. In Table III we list the results of the wavelet test on the same maps (for the wavelets we used the parameter $R=22.5'$). For individual results of the empirical process test, we refer to [30].

Table IV shows the number of detections at the different levels, using M_0 and the empirical process method on maps with $f_{NL}=100$ and $f_{NL}=300$. The power of the two procedures appears very close. However, analyzing the individual maps, we find that only one-third of the maps detected at 2σ are the same for the two tests. This leads to the idea of

TABLE II. The quantile levels which determine the 1σ and 2σ detections and the rejection rates for nonstandard inflationary models with $f_{NL}=100$.

Quantile detection limits								
I_0	1σ	3.6×10^{-3}	I_1	1σ	0.286	I_2	1σ	33.2
	2σ	6.3×10^{-3}		2σ	0.524		2σ	49.7
Rejection rates (%)								
I_0	1σ	68	I_1	1σ	52	I_2	1σ	57
	2σ	35		2σ	8		2σ	8

TABLE III. Wavelets test: the rejection rates at 1σ and 2σ for nonstandard inflationary models with $f_{NL}=100$.

Confidence level	Rejection rate
1σ	89%
2σ	57%

implementing a combined test.

For the combined test we suggest using an indicator consisting of I_0 from the Minkowski functionals and $k_{\max}$ from the empirical process. We chose to normalize the I_0 and $k_{\max}$ so that they both have mean zero and variance 1, using Monte Carlo simulations of Gaussian maps. In this way, the two values can be averaged:

$$x = w_1 \tilde{I}_0 + w_2 \tilde{k}_{\max}, \tag{17}$$

where

$$\tilde{I}_0 = (I_0 - \langle I_0 \rangle)/\sqrt{\langle I_0^2 \rangle - \langle I_0 \rangle^2}, \tag{18}$$

and

$$\tilde{k}_{\max} = (k_{\max} - \langle k_{\max} \rangle)/\sqrt{\langle k_{\max}^2 \rangle - \langle k_{\max} \rangle^2}. \tag{19}$$

Here $\langle\rangle$ means the mean value taken over 100 Gaussian simulations. The weights w_1 and w_2 were chosen proportionally to the power of each procedure. Using the rejection rates for $f_{NL}=100$ in Table II, we arrived at $w_1 \approx 0.6$ and $w_2 \approx 0.4$. Of course, the threshold value for x needs to be evaluated anew. In Fig. 6 we plot the distribution of x for the Gaussian and $f_{NL}=100$ non-Gaussian maps.

With a similar motivation, it is natural to combine the wavelet method also into a single procedure; it is easy to see (Tables II and III) that the detection rate at 2σ is about twice higher for the wavelets, justifying a very high weight for the wavelet coefficient in the combined analysis. Inspecting Table IV, we detect a moderate improvement in the detection rate when combining Minkowski functionals and the empirical process. The result of the empirical process + Minkowski functionals + wavelets combined test is shown in Table V. A significant improvement of the number of detections at both confidence levels is evident; note that the combined procedure is to some extent model dependent, as the weights we used were tabulated from specific non-Gaussian models.

TABLE IV. Comparison and combined test.

	Test				
	Empirical process		M_0		Combination
f_{NL}	100	300	100	300	100
1σ	50%	95%	68%	100%	74%
2σ	29%	87%	35%	100%	35%

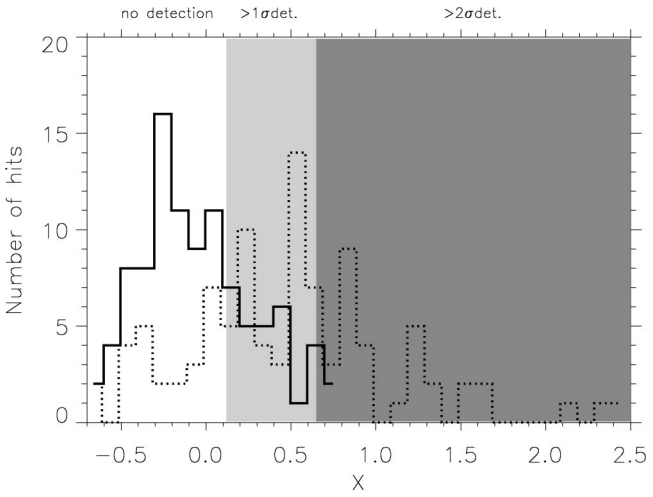

FIG. 6. Histogram of the combined estimator x (empirical process and Minkowksi functionals) for Gaussian realizations (solid line) and non-Gaussian realizations with $f_{NL}=100$ (dotted line). All realizations have Planck-like noise and beam $20'$. The shaded areas represent the 1σ and 2σ detection limits.

VIII. POINT SOURCES

We also simulated maps with point sources (with noise and beam as given above) to compare the power of the methods on a different kind of non-Gaussianity. We generated a toy model of point sources with a distribution building on formula (1) in [41] and formulas (1) and (2) in [42]. In Table VI we show the results for the Minkowski functionals. We see immediately that for this kind of non-Gaussianity the first Minkowski functional is not sensitive, whereas the other two functionals show a good rejection rate. This suggests that we might be able to discriminate between these two types of non-Gaussianity. The first Minkowski functional can be used to trace primordial non-Gaussianity with little influence from the point sources. On the other hand, the presence of point sources will show up in the second and third Minkowski functionals, which are only weakly influenced by primordial non-Gaussianity. In Fig. 7 we show the shape of the Minkowski functionals in the presence of point sources. Note that the deviations from the Gaussian mean are different from those in the case of primordial non-Gaussianity (Fig. 4). The point sources manifest themselves mainly as an offset in M_1 and M_2, consistent with what was observed for weak lensing [43]. However, as seen in Fig. 5 for nonstandard inflation the curve has a particular shape.

One could imagine combining M_1 and M_2 in order to strengthen the power of the test, similarly to what we have done above. However, it turns out that the maps detected by

TABLE V. The results of the combined test using all three methods, empirical process, Minkowski functionals, and wavelets, for $f_{NL}=100$.

Confidence level	Rejection rate
1σ	100%
2σ	78%

TABLE VI. The quantile levels which determine the 1σ and 2σ detections and the rejection rates for maps contaminated by point sources.

Quantile detection limits								
I_0	1σ	1.1×10^{-3}	I_1	1σ	0.415	I_2	1σ	207.6
	2σ	1.7×10^{-3}		2σ	0.770		2σ	328.3
Rejection rates (%)								
I_0	1σ	36	I_1	1σ	81	I_2	1σ	75
	2σ	8		2σ	45		2σ	33

M_2 are contained within the maps detected by M_1, so that there is no additional information in combining the two estimators.

For the empirical process method, there was no detection for any of the tests, univariate, bivariate, or trivariate. The numbers $k_{\max}$ obtained for the maps with point sources were consistent with those for Gaussian maps. For the wavelet test also, the number of detections was very small. Note that wavelets can be useful for detection of bright point sources [44], but in our source model these were excluded. This might suggest that the empirical process methods and the skewness of the wavelets can be used to probe primordial non-Gaussianity without confusion from point sources, making the combined test presented above more robust.

IX. COMMENTS AND CONCLUSIONS

We have compared three methods for detecting non-Gaussianity in observations of the cosmic microwave background. The methods were applied to non-Gaussian maps

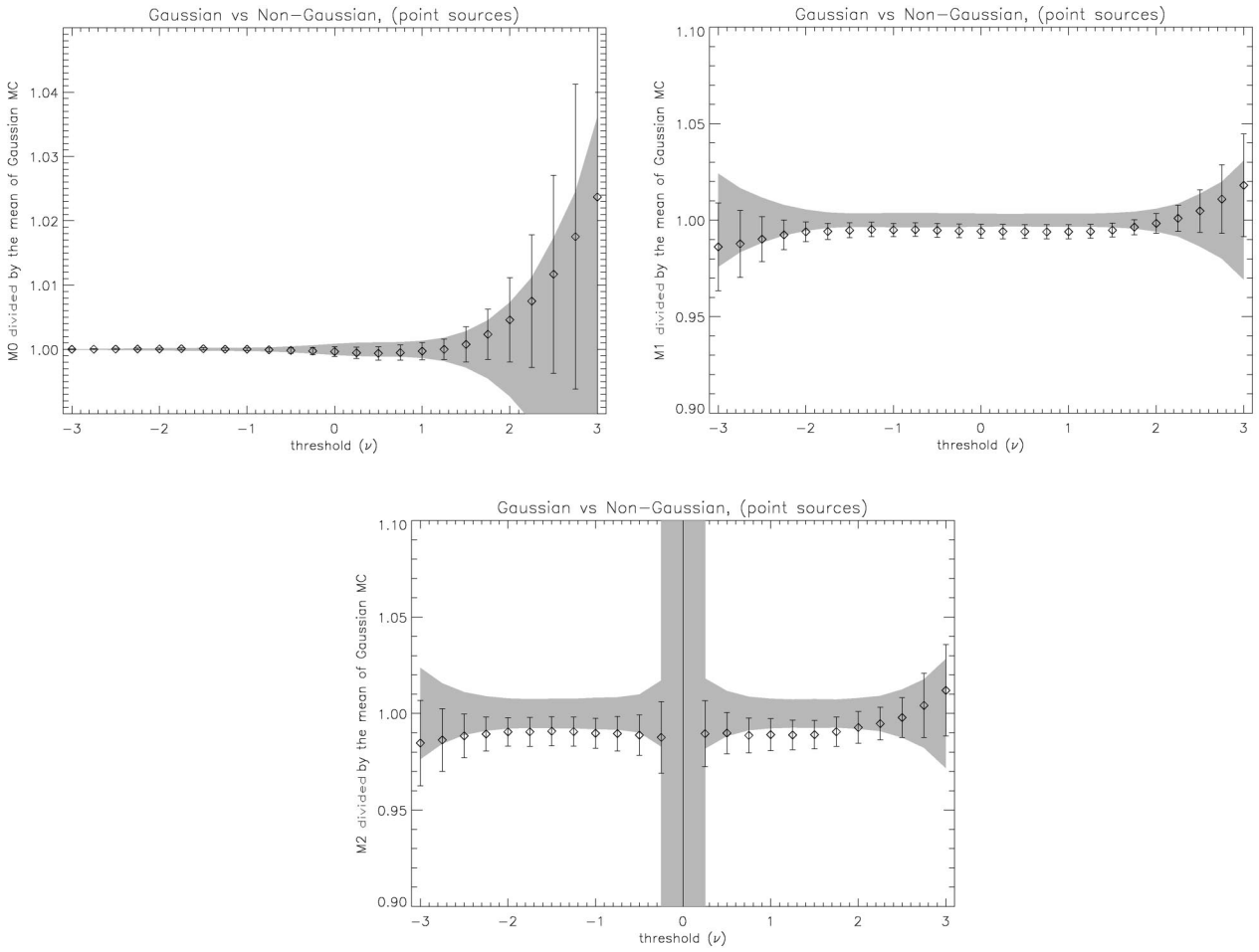

FIG. 7. Minkowski functionals (divided by the mean) averaged over 200 realizations of Gaussian maps (solid line) and 100 non-Gaussian maps (squares) with point sources, Planck noise, and beam $20'$. The shaded bands show the 1σ deviations of the Gaussian realizations and the error bars show the 1σ deviations for the non-Gaussian maps.

with two different kinds of non-Gaussianity, primordial non-Gaussianity with a varying f_{NL} and point sources. It is important to note that the non-Gaussian maps used in this article were generated taking into account only the Sachs-Wolfe effect. In future work we will study maps where the full radiative transfer equations have been applied. For the time being, we stress that our results are broadly consistent with the power of the procedures adopted for WMAP data analysis. More precisely, a detailed comparison is not feasible, as we are assuming a simplified non-Gaussian model (no radiative transfer) and Planck LFI-like noise and beam. Moreover, we are restricting the analysis to the first 500 multipoles. Broadly speaking, however, Monte Carlo simulations suggest that a value of f_{NL} about 100 represents the lower limit that can be detected at a 2σ level, by using a combined procedure: this seems consistent with the value $f_{NL}=139$ reported in [11]. As an estimator of non-Gaussianity for the Minkowski functionals we have introduced a statistic which gathers the information from different thresholds [Eq. (10)]. The estimator for the empirical process method is $k_{\max}$, the maximum value of the function $K(\alpha,r)$ obtained from a given map [Eq. (11)] using the trivariate test. For the test in wavelet space, we use the skewness of wavelet coefficients.

For the primordial non-Gaussianity, M_0 and the empirical process method have a similar rejection rate, whereas M_1 and M_2 showed less power. On the other hand, for the maps with point sources, M_1 and M_2 gave the best results, whereas M_0 and the empirical process method had no rejections. The fact that the first Minkowski functional shows little power in the presence of point sources is hardly surprising. Indeed, this statistic depends only on the pixel by pixel temperature values and hence is not at all affected by discontinuities in the map. The converse is clearly true for the other Minkowski functionals, which are sensitive to the local morphology of the maps. For the empirical process, we simply note that spikes in real space are erased in harmonic space. It is also important to stress that our results depend heavily upon the nature of non-Gaussianity; in particular, some preliminary exploration of Monte Carlo evidence from non-physical toy models suggests that the power of these procedures need not be close, in general. This strengthens the case for (weighted) multiple/combined procedures; the combined procedures seem to show a marked improvement in the power of the test. However, the pixel, harmonic, and wavelet space methods, despite carrying complementary statistical information, should not be viewed either as orthogonal or as independent, so that some care is needed when merging them into a single statistic. In any case, the fact that different methods detect different kinds of non-Gaussianity can be viewed as an advantage, in the sense that, for instance, primordial non-Gaussianity can be detected without confusion from point sources.

ACKNOWLEDGMENTS

We are thankful to Michele Liguori and Sabino Matarrese for supplying maps with primordial non-Gaussianity. We also wish to thank Paolo Natoli for suggestions and useful discussions. This research used resources of the National Energy Research Scientific Computing Center, which is supported by the Office of Science of the U.S. Department of Energy under Contract No. DE-AC03-76SF00098. We acknowledge the use of the HEALPIX package [40].

[1] J. Martin, A. Riazuelo, and M. Sakellariadou, Phys. Rev. D **61**, 083518 (2000).
[2] C.R. Contaldi, R. Bean, and J. Magueijo, Phys. Lett. B **468**, 189 (2000)
[3] A. Linde and V. Mukhanov, Phys. Rev. D **56**, 535 (1997).
[4] S. Gupta, A. Berera, A.F. Heavens, and S. Matarrese, Phys. Rev. D **66**, 043510 (2002).
[5] A. Gangui, J. Martin, and M. Sakellariadou, Phys. Rev. D **66**, 083502 (2002).
[6] N. Bartolo, S. Matarrese, and A. Riotto, Phys. Rev. D **65**, 103505 (2002).
[7] M. Liguori, S. Matarrese, and L. Moscardini, Astrophys. J. **597**, 57 (2003).
[8] A. Gangui, L. Pogosian, and S. Winitzki, Phys. Rev. D **64**, 043001 (2001).
[9] D. Novikov, J. Schmalzing, and V.F. Mukhanov, Astron. Astrophys. **364**, 17 (2000).
[10] J.R. Gott *et al.*, Astrophys. J. **352**, 1 (1990).
[11] E. Komatsu *et al.*, Astrophys. J., Suppl. Ser. **148**, 119 (2003).
[12] H.K. Eriksen, A.J. Banday, and K.M. Górski, Astron. Astrophys. **395**, 409 (2002).
[13] A.F. Heavens and S. Gupta, Mon. Not. R. Astron. Soc. **324**, 960 (2000).
[14] R. Scaramella and N. Vittorio, Astrophys. J. **375**, 439 (1991).
[15] O. Doré, S. Colombi, and F.R. Bouchet, Mon. Not. R. Astron. Soc. **344**, 905 (2003).
[16] R.B. Barreiro, E. Martinez-Gonzalez, and J.L. Sanz, Mon. Not. R. Astron. Soc. **322**, 411 (2001).
[17] N.G. Phillips and A. Kogut, Astrophys. J. **548**, 540 (2000).
[18] E. Komatsu, B.D. Wandelt, D.N. Spergel, A.J. Banday, and K.M. Górski, Astrophys. J. **566**, 19 (2002).
[19] E. Komatsu and D.N. Spergel, Phys. Rev. D **63**, 063002 (2001).
[20] G.D. Troia *et al.*, Mon. Not. R. Astron. Soc. **313**, 284 (2003).
[21] S. Winitzki and J.H.P. Wu, astro-ph/0007213.
[22] W. Hu, Phys. Rev. D **64**, 083005 (2001).
[23] M. Kunz *et al.*, Astrophys. J. Lett. **563**, L99 (2001).
[24] L.Y. Chiang, P. Naselsky, and P. Coles, astro-ph/0208235.
[25] J.H. Wu *et al.*, Phys. Rev. Lett. **87**, 251303 (2001).
[26] G. Polenta *et al.*, Astrophys. J. Lett. **572**, L27 (2002).
[27] P.G. Ferreira, J. Magueijo, and K.M. Górski, Astrophys. J. Lett. **503**, L1 (1998).
[28] A.J. Banday, S. Zaroubi, and K.M. Górski, Astrophys. J. **533**, 575 (2000).
[29] F.K. Hansen, D. Marinucci, P. Natoli, and N. Vittorio, Phys. Rev. D **66**, 063006 (2002).
[30] F.K. Hansen, D. Marinucci, and N. Vittorio, Phys. Rev. D **67**, 123004 (2003).

[31] D. Marinucci and M. Piccioni, Ann. Stat. **32**, 3 (2004).
[32] R.B. Barreiro and M.P. Hobson, Mon. Not. R. Astron. Soc. **327**, 813 (2001).
[33] R.B. Barreiro, M.P. Hobson, A.N. Lasenby, A.J. Banday, K.M. Gorski, and G. Hinshaw, Mon. Not. R. Astron. Soc. **318**, 475 (2000).
[34] E.M. Gonzalez, J.E. Gallegos, F. Argueso, L. Cayon, and J.L. Sanz, Mon. Not. R. Astron. Soc. **336**, 22 (2002).
[35] P. Mukherjee, M.P. Hobson, and A.N. Lasenby, Mon. Not. R. Astron. Soc. **318**, 1157 (2000).
[36] H. Minkowski, Math. Ann. **57**, 447 (1903).
[37] K.J. Worsley, Adv. Appl. Probab. **26**, 13 (1994).
[38] J. Schmalzing and K.M. Górski, Mon. Not. R. Astron. Soc. **297**, 355 (1998).
[39] H. Tomita, in *Formation, Dynamics and Statistics of Patterns*, Vol. 1, edited by K. Kawasaki, M. Suzuki, and A. Onuki (World Scientific, Singapore, 1990), pp. 113–157.
[40] K.M. Górski, E. Hivon, and B.D. Wandelt, in *Analysis Issues for Large CMB Data Sets*, edited by A.J. Banday, R.K. Sheth, and L. Da Costa (ESO Printpartners Ipskamp, Netherlands, 1998), pp. 37–42.
[41] E. Pierpaoli, Astrophys. J. **589**, 58 (2003).
[42] M. Tegmark and A. de Oliveira-Costa, Astrophys. J. Lett. **500**, L83 (1998).
[43] J. Schmalzing, M. Takada, and T. Futamase, Astrophys. J. Lett. **544**, L83 (2000).
[44] L. Cayón *et al.*, Mon. Not. R. Astron. Soc. **315**, 757 (2000).
[45] H. Hadwiger, Math. Z. **71**, 124 (1959).
[46] S. Winitzki and A. Kosowsky, New Astron. **3**, 75 (1998).